

# Optimisation of hybrid high-modulus/high-strength carbon fiber reinforced plastic composite drive

O. Montagnier<sup>a,b,\*</sup>, C. Hochard<sup>b</sup>

<sup>a</sup>Centre de recherche de l'Armée de l'air (CREA), Laboratoire de Dynamique du Vol, BA 701, 13361 Salon Air, France

<sup>b</sup>Laboratoire de Mécanique et d'Acoustique (LMA), 31 chemin Joseph Aiguier, 13402 Marseille Cedex 20, France

---

## Abstract

This study deals with the optimisation of hybrid composite drive shafts operating at subcritical or supercritical speeds, using a genetic algorithm. A formulation for the flexural vibrations of a composite drive shaft mounted on viscoelastic supports including shear effects is developed. In particular, an analytic stability criterion is developed to ensure the integrity of the system in the supercritical regime. Then it is shown that the torsional strength can be computed with the maximum stress criterion. A shell method is developed for computing drive shaft torsional buckling. The optimisation of a helicopter tail rotor driveline is then performed. In particular, original hybrid shafts consisting of high-modulus and high-strength carbon fibre reinforced epoxy plies were studied. The solutions obtained using the method presented here made it possible to greatly decrease the number of shafts and the weight of the driveline under subcritical conditions, and even more under supercritical conditions. This study yielded some general rules for designing an optimum composite shaft without any need for optimisation algorithms.

*Keywords:* Drive shaft, Optimisation, Hybrid carbon fibre reinforced plastic

---

## 1. Introduction

Since the 1970s, composite materials have been regarded as potential candidates for manufacturing drive shafts because of their high specific stiffness and strength [1]. Previous studies on this topic have dealt mainly with composite shaft design in the subcritical case, that is when the first critical speed is never exceeded. However, when a long driveline is required (in the case of helicopters, tilt-rotors, tailless aircraft with twin turboprops, etc.), an additional means of increasing the drive shaft length consists in operating above the first critical speed, in the so-called supercritical regime. The main advantage of long shafts is that they reduce the number of bearing supports required, and thus greatly decrease the maintenance costs and the weight of the driveline. The design process is more complex, however, because the shaft has to cross a critical speed, and dynamic instabilities due to rotating damping can occur in this regime. Aeronautic applications lend themselves well to operating in the supercritical regime because the driveline always rotates at the nominal speed during flight, since they undergo acceleration and deceleration processes on the ground. The aim of this paper is to optimise a supercritical drive shaft in this practical case.

Many different numerical methods have been used to design optimised composite drive shafts in order to reduce their weight, for

example. Traditional methods based on the gradients of continuous functions have been used for this purpose by several authors [2–4]. These methods are unsuitable in the case of composite laminates, however, because many of the variables which have to be optimised are discrete variables (such as the number of plies and the ply angle in prepreg lay-up processes). It is therefore necessary to assume these variables to be continuous to be able to compute the gradients required. The optimisation techniques available for solving problems involving discrete variables are known as metaheuristic methods. For example, Gubran and Gupta [5] have used simulated annealing techniques based on a neighbourhood approach. A review of the literature shows that genetic algorithms (GA) [6, 7] are well adapted to designing laminate structures. GA were recently used to optimise a flexible matrix composite drive shaft in [8]. Here it is proposed to use a GA with penalisation methods to account for the constraint functions. In addition, in order to reduce the CPU time, all the design aspects are handled without requiring the use of finite element methods.

In drive shaft applications, the choice of composite material is of great importance. Several authors have recommended the use of hybrid composites in the production of drive shafts. Xu et al. [9], Gubran [10], and Badie et al. [11] recently studied the advantages of a mixture of glass and carbon fibres in a modified epoxy matrix. Lee et al. [12], Gubran [10], Mutasher [13] and Abu Talib et al. [14] recently have studied the design and manufacture of hybrid metallic/composite drive shafts. Here it is proposed to study the use of

---

\* Corresponding author. Tel. : (+33)4.90.17.80.93 ; fax : (+33)4.90.17.81.89.  
 Email address: olivier.montagnier@inet.air.defense.gouv.fr  
 (O. Montagnier)

## Nomenclature

<b>A</b> , $A_{ij}$	in-plane stiffness matrix of the laminate and elements of the matrix ( $i, j = 1, 2, 6$ )	<b>x, y, z</b>	coordinates
<b>a</b> , $a_{ij}$	in-plane compliance matrix of the laminate and elements of the matrix	$\alpha$	orientation of the ply
<b>B</b> , $B_{ij}$	coupling stiffness matrix of the laminate and elements of the matrix	$\eta$	loss factor
$c$	viscous damping	$\kappa$	shear coefficient
<b>D</b> , $D_{ij}$	flexural stiffness matrix of the laminate and elements of the matrix	$\nu$	Poisson's ratio of the shaft
$E$	longitudinal Young's modulus of the shaft	$\nu$	distribution of the torsional modes
$E_{11}, E_{22}$ ,	longitudinal and transverse Young's modulus, Poisson's ratio, out-of-plane (transverse / normal, longitudinal / normal) and in-plane shear modulus of the ply	$\rho$	mass density of the shaft
$E_{12}, E_{44}$ ,		$\varphi$	angular position
$E_{55}, E_{66}$		$\theta$	out-of plane cross-section rotation (complex or real)
$f$	fitness function	$\sigma_{11}, \sigma_{22}$ ,	in-plane stress of the ply (longitudinal, transverse and shear)
$G$	transverse shear modulus of the shaft	$\sigma_{12}$	
$g$	constraint function	$\omega$	natural frequency of the torsional modes
$h$	number of half-wave along the circumference	$\omega$	natural frequency of the flexural modes
$I_y, I_z$	transverse area moments of inertia of the shaft	$\Omega$	spin speed
$J$	polar mass moment of inertia		
<b>K</b>	buckling stiffness matrix	<i>Subscript</i>	
$K$	reserve factors	B-, B+,	lower and higher backward whirl speeds
$k$	stiffness	b	bearing
$l$	unsupported shaft section length	buck	buckling
$m$	mass	c	critical
$n$	number of plies	dv	driveline
$P$	power	e	external
$p$	number of half-wave along the axis	eq	equivalent
$q$	number of possible orientations in the staking sequence	F-, F+	lower and higher forward whirl speeds
$r$	shaft radius	f	flexural modes
$S$	cross-section area of the shaft	G	gear
$t$	thickness or time	i	internal
$T$	axial torque	inf	inferior
$u, v, w$	displacements (complex or real)	m	medium
$X, X', Y, Y'$ ,	tensile and compressive longitudinal strength, tensile and compressive transverse strength, in-plane shear strength	min	minimum
$s$		mat	material of a ply
		nom	nominal
		$n$	number of sine modes
		ply	laminate ply
		s	shaft
		sup	superior
		T	tail rotor
		t	torsional modes
		th	threshold speed
		str	strength

a combination of high-modulus (HM) and high-strength (HS) carbon fibre reinforced epoxy plies, in order to benefit from the main advantages of each type of fibre. The main design considerations in the case of composite laminate tubes are the axial stiffness and the torsional resistance. In this particular case, the plies providing stiffness and strength can be considered practically separately [15]. HM carbon/epoxy, which have poor strength properties, especially when exposed to compression loads [16], can serve to maximise the axial stiffness. HS carbon/epoxy can be used to maximise the resistance to torsion loads. Note that the hybridization can be simply obtained by using the same resin with both fibres. Otherwise, it would be necessary to verify the compatibility of the two resins (in terms of their curing cycle behaviour, adhesiveness, etc.). For the sake of convenience, this point is not taken into account here.

The first part of this paper presents various design aspects. In particular, the dynamic of a drive shaft is studied at supercritical speeds. The failure strength analysis focuses on the choice of the stress criterion. A composite shell model is then developed for the

torsional buckling. In the second part, the GA is presented. The last part presents a comparative study between HM and hybrid solutions on a helicopter tail rotor driveline previously presented in the literature.

## 2. Design aspects

### 2.1. Flexural vibration analysis

When designing supercritical shafts, the external damping has to be maximised in order to reduce the flexural imbalance responses and increase the stability in the supercritical regime. Rolling-element bearings provide insufficient damping. Dissipative materials such as elastomers have recently been used as bearing supports as a passive means of enhancing the non-rotating damping [17, 18]. A low cost configuration consisting of an axisymmetric composite shaft simply supported on classical rolling-element bearings mounted on viscoelastic supports was studied here (Fig. 1).

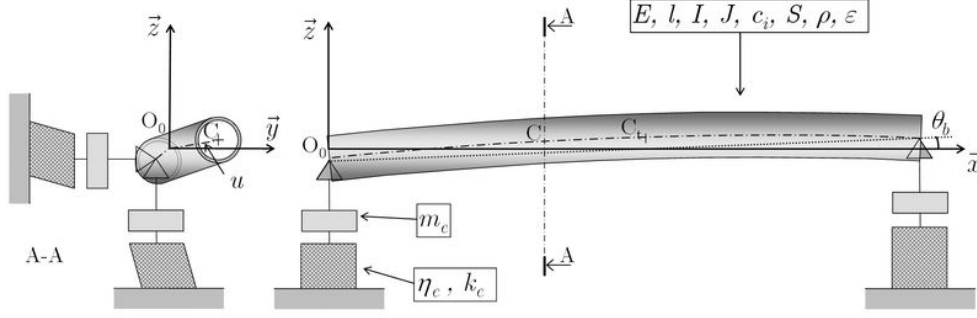


Figure 1: A simply supported axisymmetric tubular composite shaft with rolling-element bearings mounted on viscoelastic supports

Table 1: Material properties corresponding to a volume fraction of 0.6

Material	Abbr.	$\rho$ kg m <sup>-3</sup>	$E_{11}$ GPa	$E_{22}$ GPa	$E_{66}$ GPa	$E_{12}$ -	$X$ MPa	$X'$ MPa	$Y$ MPa	$Y'$ MPa	$s$ MPa	$t_{ply}$ mm
Narmco 5505 [1]	BE <sup>a</sup>	1965	211	24.1	6.89	0.36	1365	1586	45	213	62	0.1321
T300/5208 [3, 4]	CE <sub>L</sub>	1680	181	10.3	7.17	0.28	1500	1500	40	246	68	
K63712/M10 [16]	HM	1700	370	5.4	4.0	0.3	1500	470	35	200	75	0.125
T800/G947	HS	1530	162	10	5.0	0.3	2940	1570	60	290	100	0.125

<sup>a</sup> BE : boron/epoxy ; CE : carbon/epoxy

Various approaches based on beam and shell theories have been used to compute the critical speeds of composite shafts [19–21], most of which were placed on infinitely rigid supports. The simplest of these theories is called the Equivalent Modulus Beam Theory (EMBT) [1]. Based on this approach, it is proposed to investigate a rotating beam with Timoshenko's assumptions [22], replacing the isotropic properties of the material by the homogenised properties of the composite. These equations are also adapted to account for the motion of the supports and the internal damping terms. Lastly, the three complex governing equations and boundary conditions used can be written in the following form:

$$\ddot{u} - \frac{I_y}{S} \left(1 + \frac{E}{\kappa G}\right) \ddot{u}_s'' + i\Omega \frac{I_x}{S} \dot{u}_s'' + \frac{EI_y}{\rho S} u_s'''' + \frac{c_i}{\rho S l} (\dot{u}_s - i\Omega u_s) = 0, \quad (1)$$

$$\int_0^l \rho S \ddot{u} dx + 2m_b \ddot{u}_b + 2c_e \dot{u}_b + 2k_e u_b = 0, \quad (2)$$

$$\int_0^l \rho S \left(x - \frac{l}{2}\right) \ddot{u} dx + 2m_b \frac{l^2}{4} \ddot{\theta}_b + 2c_e \frac{l^2}{4} \dot{\theta}_b + 2k_e \frac{l^2}{4} \theta_b = 0, \quad (3)$$

$$u_s''(0, t) = u_s''(l, t) = 0, \quad u_s(0, t) = u_s(l, t) = 0 \quad (4)$$

where  $' = \partial / \partial x$ ,  $\dot{\ } = \partial / \partial t$ ,  $\rho = m_s / Sl$ ,  $u = u_y + iu_z$  is the cross-sectional displacement and  $u_b = u_{by} + iu_{bz}$  is the deflection of the shaft (see the list of nomenclature for the other parameters). Using the method presented in [18], the above equations yield the four critical speeds for the  $n$ th harmonic:

$$\omega_{cnF\pm} = \frac{1}{\sqrt{2\Delta_{n-}}} \left[ \omega_{sn}^2 + \Lambda_{n-} \omega_{bn}^2 \pm \sqrt{\omega_{sn}^4 + 2(\Lambda_{n-} - 2\Delta_{n-}) \omega_{sn}^2 \omega_{bn}^2 + \Lambda_{n-}^2 \omega_{bn}^4} \right]^{1/2} \quad (5)$$

$$\omega_{cnB\pm} = -\frac{1}{\sqrt{2\Delta_{n+}}} \left[ \omega_{sn}^2 + \Lambda_{n+} \omega_{bn}^2 \pm \sqrt{\omega_{sn}^4 + 2(\Lambda_{n+} - 2\Delta_{n+}) \omega_{sn}^2 \omega_{bn}^2 + \Lambda_{n+}^2 \omega_{bn}^4} \right]^{1/2} \quad (6)$$

where

$$\omega_{sn}^2 = \frac{n^4 \pi^4 EI_y}{\rho S l^4} = \frac{k_{sn}}{m_s}, \quad \omega_{bn}^2 = \frac{k_e}{m_b + \frac{m_s}{2(2+(-1)^n)}}, \quad \Gamma_n = \frac{n^2 \pi^2 I_x}{S l^2},$$

$$\Pi_n = 1 + \frac{n^2 \pi^2 I_y}{S l^2} \left(1 + \frac{E}{\kappa G}\right), \quad \Phi_n = \frac{m_s}{m_b + \frac{m_s}{2(2+(-1)^n)}},$$

$$\Psi_n = \Pi_n - \frac{4}{n^2 \pi^2} \Phi_n, \quad \Delta_{n\pm} = \Psi_n \pm \Gamma_n, \quad \Lambda_{n\pm} = \Pi_n \pm \Gamma_n \quad (7)$$

In addition, in the case of a composite shaft consisting of a symmetric laminate, the homogenised properties can be computed with the following equations:  $E = 1/a_{11} t_s$ ,  $G = 1/a_{66} t_s$  and  $\nu = -a_{12}/a_{11}$  where  $\mathbf{a} = \mathbf{A}^{-1}$  [23]. It is also assumed that  $\kappa = 2(1 + \nu)/(4 + 3\nu)$ .

In the field of rotordynamics, internal damping, which is also referred to as rotating damping, is known to cause whirl instability in the supercritical regime. In the literature, the internal damping resulting from dissipation in the shaft material and dry friction between the assembled components has been usually approached using the viscous damping model. However, most materials, such as carbon/epoxy materials in particular, show vibratory damping, which resembles hysteretic damping much more than viscous damping [24, 25]. Using the classical equivalence between viscous and hysteretic damping [18], the analytical instability criterion suitable for shaft optimisation purposes, can be written in the following form:

$$\pm \left( \eta_e k_e \Phi_n (\Pi_n \omega_{nF\pm}^2 - \omega_{sn}^2) - \eta_i k_{sn} (\omega_{nF\pm}^2 - \omega_{bn}^2) \right) \begin{cases} < 0 & \Rightarrow \omega_{thnF\pm} = \omega_{nF\pm} \\ \geq 0 & \Rightarrow \text{stable} \end{cases} \quad (8)$$

where

$$\omega_{nF\pm} = \frac{1}{\sqrt{2\Psi_n}} \left[ \omega_{sn}^2 + \Pi_n \omega_{bn}^2 \pm \sqrt{\omega_{sn}^4 + 2(\Pi_n - 2\Psi_n) \omega_{sn}^2 \omega_{bn}^2 + \Pi_n^2 \omega_{bn}^4} \right]^{1/2} \quad (9)$$

and where the equivalent longitudinal loss factor denoted  $\eta_i$  is computed with Adams, Bacon and Ni's theory [26, 27] using complex

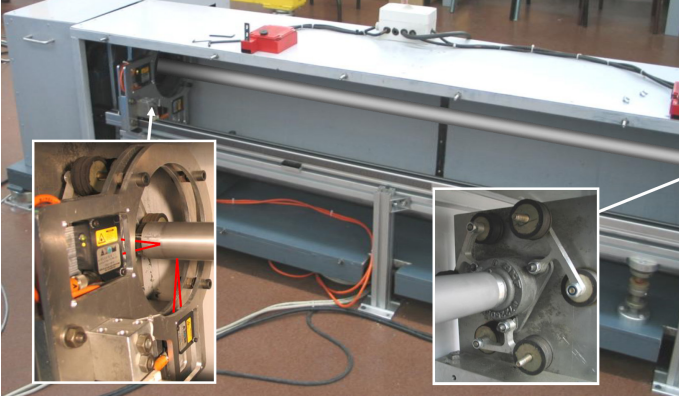


Figure 2: The dynamic shaft test rig: the zoom image (left) corresponds to the non-contact laser-optical displacement sensors (with the scheme of the laser beams in red), the detail (right) corresponds to the bearing mounted on the six viscoelastic supports (the left plate was removed to take the snapshot).

properties of the ply ( $\eta_{11} = 0.11\%$ ,  $\eta_{22} = 0.70\%$  and  $\eta_{66} = 1.10\%$ ). It then suffices to compute the lowest threshold speed in order to determine the spin speed limit of the shaft.

A dynamic shaft test rig corresponding to the case of Fig. 1 has been developed to validate the theoretical results (Fig. 2). Basically, the test rig consists in a shaft that is powered by an electric motor via a belt and pulley system and is capable of a maximum test velocity of 12 000 rpm. Two non-contact laser-optical displacement sensors are able to measure the cross-section displacement in real-time. The detailed characteristics of the test rig are given in [25, 28]. In the case of a long aluminium shaft ( $E = 69$  GPa,  $\rho = 2700$  kg.m<sup>-3</sup>,  $l = 1.80$  m,  $r_m = 23.99$  mm,  $t = 2.02$  mm) supported on viscoelastic supports ( $m_b = 2.817$  kg,  $k_e = 5.64 \times 10^5$  N.m<sup>-1</sup>), the critical speeds  $\omega_{c1F-}$  and  $\omega_{c1F+}$  were measured to be 251 rad.s<sup>-1</sup> and 446 rad.s<sup>-1</sup>, respectively. The results obtained with the above model are 250 rad.s<sup>-1</sup> and 460 rad.s<sup>-1</sup> which is very close to the experiment.

The experimental investigation of the instabilities can initiate catastrophic risks for the dynamic test rig. For this reason, it was proposed to study the instabilities using PVC material. Another advantage of the PVC material is its low stiffness and high damping ( $E = 2.2$  GPa,  $\rho = 1350$  kg.m<sup>-3</sup> and  $\eta_i = 0.025\%$ ) which decrease the critical and threshold speeds. Several shafts with four different lengths were tested in the supercritical domain ( $r_m = 23.25$  mm,  $t = 2.5$  mm with  $m_b = 2.608$  kg,  $k_e = 2.58 \times 10^5$  N.m<sup>-1</sup> and  $\eta_e = 0.07\%$ ). A high level of acceleration was required in order to run over the first critical speed. Only the shafts of length 0.8 m and 0.9 m were found to be stable in the supercritical regime. The theoretical model is compared to experimental results in the Fig. 3. A relatively good correlation is obtained considering these experiments are difficult to achieve. Note that the stability area is obtained at the intersection of the rigid body mode and the first flexural mode ( $l = 0.85$  m).

## 2.2. Torsional vibration analysis

Torsional vibrations are computed using classical methods with the relations presented by Lim and Darlow [3]:

$$\omega_n = \frac{v_n}{l} \sqrt{\frac{G}{\rho}} \quad (10)$$

with

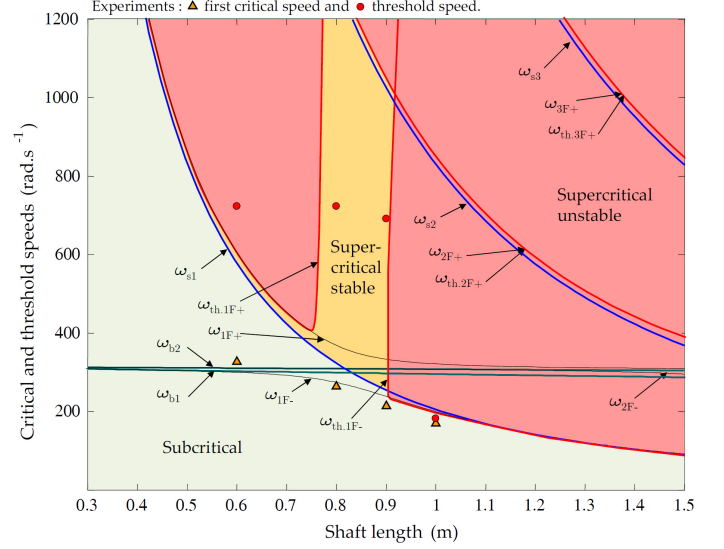


Figure 3: The theoretical uncoupled natural frequencies ( $\omega_{sn}$ ,  $\omega_{bn}$ ), forward critical speeds ( $\omega_{nF\pm}$ ) and threshold speeds ( $\omega_{th,nF\pm}$ ) vs. experimental data in the case of tubes in PVC material of various length.

$$v_1 \approx \sqrt{2} \sqrt{\frac{J_G J_s + J_T J_s + J_s^2}{J_G J_s + J_T J_s + 2J_G J_T}}$$

$$v_{n \neq 1} \approx \frac{(n-1)\pi}{2} + \sqrt{\frac{(n-1)^2 \pi^2}{4} + \frac{J_s}{J_T} + \frac{J_s}{J_G}}$$

where  $J_G$ ,  $J_T$  and  $J_s$  are the mass moment of inertia of the main gear, the tail rotor and the shaft, respectively.

## 2.3. Failure strength analysis

Only the torsional resistance of the shaft is taken into account here. The transmitted torque causes only in-plane shear, which can be computed with classical laminate theory [23]. Contrary to what occurs with an unsymmetrical free-edge laminate plate, the tubular structure blocks the coupling effects in the case of small displacements. This can be modelled simply by assuming the classical coupling matrix  $\mathbf{B}$  to be null before performing the inversion procedure required to compute the strain state.

A conservative approach often used in the case of helicopter drive shafts consists in computing only the fracture of the first ply. The Tsai-Wu criterion [29] can be used in this case to account for the differences between the tensile and compressive strengths, which can be of great importance in the case of HM carbon/epoxy (see Table 1):

$$\frac{1}{XX'} \sigma_{11}^2 + 2 \frac{F_{12}}{\sqrt{XX'YY'}} \sigma_{11} \sigma_{22} + \frac{1}{YY'} \sigma_{22}^2 + \frac{1}{s^2} \sigma_{12}^2 + \left(\frac{1}{X} - \frac{1}{X'}\right) \sigma_{11} + \left(\frac{1}{Y} - \frac{1}{Y'}\right) \sigma_{22} \leq 1 \quad (11)$$

where  $F_{12}$  is an interaction parameter which is taken to be equal to 0.5. It should be noted that the Tsai-Wu criterion includes the transverse fracture mechanism. In the HS carbon/epoxy material, the transverse failure strain is approximately equal to 0.6%, while the longitudinal one is equal to 1.8%. This type of fracture generally has no direct effects on the fracture of the laminate, and this approach therefore seems to be too conservative. Assuming that the structure will be safe up to the occurrence of the first longitudinal or shear failure, a more realistic torque resistance limit can be obtained [15, 30].

This limit can be computed quite simply with a maximum stress criterion:

$$-X' \leq \sigma_{11} \leq X \quad ; \quad |\sigma_{12}| \leq s \quad (12)$$

The comparisons made in Table 2 between the results obtained with these criteria and the experimental data confirm the validity of this approach. In the case of tubes Nos. 1 and 2, the values obtained with the maximum stress criterion showed better agreement with the experimental data than those obtained using the Tsai-Wu criterion. The assumption involving the presence of a null coupling mechanism in the case of unsymmetrical laminates was also found to be true. The Tsai-Wu values could be improved by taking a greater transverse tensile strength  $Y$ .

#### 2.4. Torsional buckling analysis

Finite element methods are those most frequently employed to predict torsional buckling. However, an alternative method is presented here, which requires less computing time, and consists in solving the buckling shell problem in the case of orthotropic circular cylinders, using Flügge's buckling shell theory [32]. The laminate theory is included in the shell equations, as established in [33]. This gives the Eqs. (A.1-A.3) (see Appendix A). Since we are dealing here with very long shafts, it is possible to neglect the boundary condition effects. In this case, a simplified displacement field presented by Flügge can be used:

$$u = a \sin(h\varphi + \frac{p\pi x}{l}), \quad v = b \sin(h\varphi + \frac{p\pi x}{l}), \quad w = c \cos(h\varphi + \frac{p\pi x}{l}) \quad (13)$$

where  $(u, v, w)$  is the displacement field of the middle-surface of the cylinder,  $h$  is the number of half-waves along the cylinder's circumference and  $p$  is the number of half-waves along the axis of the cylinder with a fictive length  $l$ . When this displacement field is applied to the shell equations, a classical eigenvalue problem is obtained:

$$\mathbf{K}\mathbf{U} = \mathbf{0} \quad \text{with} \quad \mathbf{U} = \begin{bmatrix} a \\ b \\ c \end{bmatrix} \quad (14)$$

where  $\mathbf{K}$  is the stiffness matrix (the elements of  $\mathbf{K}$  are given in Appendix A). A non-trivial solution exists when the determinant of  $\mathbf{K}$  is null.

The numerical method used here consists in finding the minimum value of the buckling torque  $T_{\text{buck}}$  which cancels the determinant among all the values of  $h \in \mathbb{N}^*$  and  $p \in \mathbb{R}^{*+}$ . The computing time was reduced as follows. First, we have observed that the minimum value of the buckling torque is always obtained at  $h = 2$ . Secondly, instead of searching for the value of  $p$  between 0 and  $+\infty$ , this unknown can be found by searching around the value of  $l(48t^2/12r^2)^{1/4}/\pi r$  obtained by Flügge [32] in the case of isotropic material. Thirdly, the search for the buckling torque is conducted around the value of  $T_{\text{buck}}$ , which can be obtained with an analytic criterion such as Hayashi's criterion [31]:

$$T_{\text{buck}} = 11 \sqrt{r} \left( A_{11} - \frac{A_{12}^2}{A_{22}} \right)^{1/4} D_{22}^{3/4} \quad (15)$$

It is worth noting that this criterion, like other classical criteria, does not account for the coupling mechanism involved in unsymmetrical laminates.

The shell method was first tested on off-axis stacking sequences. The buckling torque obtained are presented in Table 3 and compared with those obtained with the finite element method, the above

criterion and by Bert and Kim [33]. The results obtained with the finite element method using ABAQUS (s4 elements) [34], which were previously validated in [25] based on experimental results obtained by Bauchau et al. [35] in the case of short tube, are taken as reference values. Bert and Kim buckling theory is based on the Sanders shell theory and take the boundary conditions into account. In the table, the results obtained by Bert and Kim correlate perfectly well with the finite element computations. Those obtained with the method presented here show higher differences which is explain by the too low length-to-diameter ratio ( $l/(2r_m) \approx 20$ ). The results show the highest differences at the extremum cases ( $0^\circ$  and  $90^\circ$ ) which yet are symmetric, however, the method is conservative. The error obtained with the Hayashi criterion can reach 82%.

The shell method was then tested on unsymmetrical stacking sequences for higher length-to-diameter ratio ( $l/(2r_m) = 50$ ) in Table 4. All the tubes presented in the table are of the same size and the laminates all have the same thickness. Buckling torque was computed in the positive and then in the negative direction. The table shows that the Hayashi criterion overestimates the buckling torque, especially in the largest unsymmetrical laminates (Nos. 9-12) by up to 40%. The results obtained with shell theory show good agreement with the finite element calculations, giving a conservative estimate on the whole. The largest errors amounted to only 8% and the mean error was 4%.

#### 2.5. Driveline mass

The driveline is composed of shafts and intermediate supports, which include bearings, fittings, and supports. The intermediate support mass  $m_b$  can be computed with an empirical equation from Lim and Darlow [3]:

$$m_b = 17.1288 \left( \frac{P_{\text{dv}}}{\Omega_{\text{nom}}} \right)^{0.69} \quad (16)$$

where  $P_{\text{dv}}$  is the power transmitted with the driveline (in W) and  $\Omega_{\text{nom}}$  is the nominal spin speed (in rev / min). The driveline's mass can then be computed using the following expression:

$$m_{\text{dv}} = N_s \times m_s + N_b \times m_b \quad \text{with} \quad m_s = \rho S l \quad (17)$$

where  $N_s$  is the number of shafts and  $N_b$  is the number of intermediate supports.

### 3. Shaft optimisation using a genetic algorithm

The principles underlying the GA algorithm are the same as those on which Darwin's theory of evolution was based. At the beginning, a randomly created population is evaluated with a fitness function. The result gives the fitness of each individual. Starting with this information, the new generation of the population can be deduced using selection, crossover and mutation operators. This process is iterated up to convergence.

The main risk with this stochastic method is that of not obtaining the optimum solution. In particular, GA may tend to converge on local optima and may not be able to cross these attracting points. Another weakness of the method is the large amount of fitness function calculations required. This means that the evaluation procedure must not be too time-consuming.

#### 3.1. Individual

An individual in this driveline optimisation procedure consists of the medium diameter  $r_m$  (which can be fixed or otherwise), the bearing stiffness  $k_e$  (fixed or not), the nominal spin speed  $\Omega_{\text{nom}}$  and

Table 2: Comparison between torque resistance calculations on various short BE tubes

Nos.		1	2	3
Stacking sequence (from inner to outer radius)	°	[90,45,-45,90]	[90,45,-45,0,90]	[90,0,2,90]
Outer radius × length	mm	25.4 × 50.8	63.5 × 305	25.4 × 50.8
Experimental [1]	N.m	581	4689 <sup>a</sup>	132
Tsai-Wu criterion	N.m	167 (-71%)	1605 (-66%)	130 (3%)
Tsai-Wu criterion with $\mathbf{B} = \mathbf{0}$	N.m	313 (-46%)	2613 (-44%)	130 (3%)
Maximum stress in fibre and shear directions	N.m	517 (-10%)	1610 (-66%)	130 (3%)
Maximum stress in fibre and shear directions with $\mathbf{B} = \mathbf{0}$	N.m	585 (2%)	4880 (4%)	130 (3%)
Buckling torque computed with Hayashi [31] criterion	N.m	1049	13 016	1547

<sup>a</sup> Mean value of two specimen tests.

Ply orientation angle	°	0	15	30	45	60	75	90
Abaqus	N.m	1 489	974	1 121	1 769	2 587	3 131	3 278
Present work	N.m (%)	966 (-35)	755 (-22)	979 (-13)	1 647 (-7)	2 445 (-5)	2 957 (-6)	2 835 (-14)
Bert & Kim	N.m (%)	1 587 (7)	974 (0)	1 126 (0)	1 790 (1)	2 617 (1)	3 156 (1)	3 016 (-8)
Hayashi criterion	N.m (%)	1 887 (27)	1 776 (82)	1 607 (43)	1 648 (-7)	2 216 (-14)	3 925 (-25)	3 365 (3)

Table 3: Comparison between buckling torque calculations on off-axis BE drive shafts ( $l = 2.47$  m,  $r_m = 62.85$  mm and  $t_s = 1.32$  mm)

the stacking sequence with various materials, symmetric or otherwise, as in the following example:  $[\alpha_1^{\text{mat}_1} \times n_1, \dots, \alpha_j^{\text{mat}_j} \times n_j, \dots, \alpha_q^{\text{mat}_q} \times n_q]$  where  $\alpha_j$ ,  $n_j$  and  $\text{mat}_j$  are the orientation, the number of plies and the material of which the ply  $j$  is made, respectively. Under supercritical conditions, the stiffness of the bearings is a necessary optimisation variable because it appears in both the rigid mode frequencies Eq. (7) and the stability criterion Eq. (8). The shaft length corresponds to the driveline length divided by the number of shafts.

There are several possible ways of modelling the chromosomes of individuals. It is proposed here to fix the number of possible orientations in the stacking sequence, denoted  $q$ . This sets the size of the chromosome in the case of a particular optimisation process, which simplifies the crossover operations. Individuals are classically represented by an array of binary numbers. The orientation  $\alpha_j$  can be written with 2 or 3 bits, standing for the sets  $\{-45, 0, 45, 90\}$  or  $\{-67.5, -45, -22.5, 0, 22.5, 45, 67.5, 90\}$  (in degree units), respectively, which correspond to realistic prepreg hand lay-up orientations. The quantity  $n_j$  is written with 2 or 3 bits corresponding to the sets  $\{1,2,3,4\}$  and  $\{1,2,3,4,5,6,7,8\}$ , respectively. The material  $\text{mat}_j$  is written with one bit to take advantage of both HM and HS carbon/epoxy, or metal and HM carbon/epoxy, for example. Lastly,  $k_e$  and  $r_m$  are bounded and generally encoded with 3 bits. For example, a shaft with the following stacking sequence  $[45_2^{\text{mat}_1}, 0_3^{\text{mat}_2}]$  (i.e.  $q = 2$ ), with  $r_m = 52$  mm and  $\Omega_{\text{nom}} = 4000$  rev / min, with the bearing stiffness fixed and where  $\alpha_j$  and  $n_j$  are encoded with 2 bits,  $r_m$  with 4 bits,  $\Omega_{\text{nom}}$  with 3 bits and  $\text{mat}_j$  with 1 bit, is defined by the following chromosome:

$$\begin{array}{cccccccccccc}
 \boxed{1} & \boxed{0} & \boxed{0} & \boxed{1} & \boxed{0} & \boxed{0} & \boxed{1} & \boxed{1} & \boxed{0} & \boxed{1} & \dots \\
 \alpha_1=45^\circ & n_1=2 & \text{mat}_1 & \alpha_2=0^\circ & n_2=3 & \text{mat}_2 & & & & & \\
 \dots & \boxed{1} & \boxed{0} & \boxed{1} & \boxed{1} & \boxed{0} & \boxed{1} & \boxed{1} & & & \\
 r_m=52 \in [30,60] & \Omega_{\text{nom}}=4000 \in [3700,4400] & & & & & & & & & 
 \end{array}$$

The string length is therefore simply  $(\text{bit}_\alpha + \text{bit}_n + \text{bit}_{\text{mat}}) \times q + \text{bit}_{k_e} + \text{bit}_{r_m} + \text{bit}_{\Omega_{\text{nom}}}$ .

### 3.2. Constraints and fitness

The mass is the optimised value generally used in driveline problems [3, 5]. In this paper, part of the fitness function is equal to the inverse of the mass of one shaft. The other part depends on the strength, buckling and dynamic constraints previously investigated

( $n \in \mathbb{N}^*$ ):

$$g_1 = \frac{K_{\text{str}} T_{\text{str}}}{T_{\text{nom}}} - 1 \geq 0 \quad \text{with} \quad K_{\text{str}} \leq 1 \quad (18)$$

$$g_2 = \frac{K_{\text{buck}} T_{\text{buck}}}{T_{\text{nom}}} - 1 \geq 0 \quad \text{with} \quad K_{\text{buck}} \leq 1 \quad (19)$$

$$g_3 = \frac{t_s}{t_{s\text{min}}} - 1 \geq 0 \quad (20)$$

$$g_{4n} = 1 - \frac{K_{\text{tinf}n} \Omega_n}{\Omega_{\text{nom}}} \geq 0 \quad \text{with} \quad K_{\text{tinf}n} \geq 1 \quad (21)$$

$$g_{5n} = \frac{K_{\text{tsup}n} \Omega_n}{\Omega_{\text{nom}}} - 1 \geq 0 \quad \text{with} \quad K_{\text{tsup}n} \leq 1 \quad (22)$$

and in the subcritical case

$$g_6 = \frac{K_{\text{fsup}1} \omega_{c1}}{\Omega_{\text{nom}}} - 1 > 0 \quad \text{with} \quad K_{\text{fsup}1} \leq 1 \quad (23)$$

or in the supercritical case

$$g_{7n} = 1 - \frac{K_{\text{finfn}} \omega_{cn}}{\Omega_{\text{nom}}} \geq 0 \quad \text{with} \quad K_{\text{finfn}} \geq 1 \quad (24)$$

$$g_{8n} = \frac{K_{\text{fsup}n} \omega_{cn}}{\Omega_{\text{nom}}} - 1 \geq 0 \quad \text{with} \quad K_{\text{fsup}n} \leq 1 \quad (25)$$

$$g_9 = \frac{K_{\text{th}} \omega_{\text{th}}}{\Omega_{\text{nom}}} - 1 \geq 0 \quad \text{with} \quad K_{\text{th}} \leq 1 \quad (26)$$

where  $g_i$  and  $K_{\dots}$  are constraint functions and reserve factors, respectively. Eq. (18) corresponds to the torsional strength constraint, which requires that the torque computed with the strength criterion multiplied by the reserve factor is smaller than the torque required. Eq. (19) is the same equation but for the torsional buckling. The other equations are those giving the dynamic constraints. Eqs. (21-22) correspond to the positioning of the nominal spin speed between torsional modal frequencies. As regards the bending modes, the constraints depend on whether the subcritical or supercritical case applies. In the first case, Eq. (23) corresponds to the subcritical assumption, i.e. the nominal spin speed multiplied by the reserve factor must be smaller than the first critical speed. In the supercritical case, Eqs. (24-25) correspond to the positioning of the nominal spin speed between the flexural critical speeds, and Eq. (26) corresponds to the stability constraint.

GAs cannot account directly for constraint functions. This prob-

**Table 4:** Comparison between buckling torque calculations on unsymmetrical CFRP drive shafts ( $l = 4$  m,  $r_m = 40$  mm,  $E_{11} = 134$  GPa,  $E_{22} = 8.5$  GPa,  $E_{66} = E_{55} = 4.6$  GPa,  $E_{44} = 4.0$  GPa,  $E_{12} = 0.29$  and  $t_s = 1.067$  mm)

Laminate		ABAQUS		Present work		Hayashi criterion	
Nos.		Mesh <sup>a</sup>	Nm	Nm	%	Nm	%
1	[15,-15] <sub>4</sub>	60-150	210	193	-8	222	6
2	[-15,15] <sub>4</sub>	60-150	214	197	-8	222	4
3	[30,-30] <sub>4</sub>	60-150	263	254	-4	283	8
4	[-30,30] <sub>4</sub>	60-150	268	259	-3	283	6
5	[45,-45] <sub>4</sub>	60-150	385	383	-1	419	9
6	[-45,45] <sub>4</sub>	60-150	385	382	-1	419	9
7	[0 <sub>2</sub> ,45,-45,45,-45,0 <sub>2</sub> ]	60-150	230	218	-5	252	10
8	[0 <sub>2</sub> ,-45,45,-45,45,0 <sub>2</sub> ]	60-150	219	208	-5	252	15
9	[0 <sub>2</sub> ,45,0,-45,0,45,-45]	30-100	358	342	-4	420	17
10	[0 <sub>2</sub> ,-45,0,45,0,-45,45]	30-100	329	315	-4	420	28
11	[0 <sub>2</sub> ,45,0 <sub>2</sub> ,-45,45,-45]	30-100	355	340	-4	440	24
12	[0 <sub>2</sub> ,-45,0 <sub>2</sub> ,45,-45,45]	30-100	313	300	-4	440	41
13	[-45,-15,15,45,15,-15,-45,45]	60-150	389	375	-4	493	27
14	[45,15,-15,-45,-15,15,45,-45]	60-150	439	449	2	493	12
15	[15,-15,-45,-15,15,45,15,-15]	60-150	219	206	-6	265	21
16	[-15,15,45,15,-15,-45,-15,15]	60-150	241	226	-6	265	10

<sup>a</sup> Number of circumferential elements - number of lengthwise elements.

lem can be overcome by using a penalisation method consisting in deteriorating the quality of an individual that violates one or more constraints, by decreasing the fitness function. The fitness function used for mass minimisation purposes can be written in the following general form:

$$f = \frac{1}{m_s} + \sum_j \gamma_j \min(0, g_j) \quad (27)$$

where  $\gamma_j$  are the penalisation factors. The reserve factors and penalisation factors are given in Table 5.

### 3.3. The genetic algorithm method

#### 3.3.1. Initialisation

The algorithm is initialised by randomly generating a population of 300-600 individuals. The number depends on the size of the problem.

#### 3.3.2. Elitism

After evaluating the population with the fitness function, the two fittest individuals, which are also called the elites, are selected and kept for the next generation.

#### 3.3.3. Scaling, selection and crossover

With the progression of the GA, the fitness of all the individuals tends to converge on that of the fittest ones. This slows down the progress of the algorithm. A windowing method [6] is used here, whereby the fitness of the lowest ranking individual is subtracted from the fitness of each individual. Two parents are then selected, based on their scaled fitness values and a multi-point crossover operation is performed. The cutting point is selected randomly. This operation gives two children, forming the next generation.

#### 3.3.4. Mutation

The mutation consists in randomly modifying the bits of the chromosomes. The probability of occurrence of the mutation must be very high to obtain a highly diverse population. But if the mutation

**Table 6:** Search parameters of the genetic algorithm

Population size	300-600
Chromosome length	24-34
Crossover probability	90%
Mutation probability	10%
Number of generation	150-40000

process is too strong, the algorithm may not converge on the optimum fitness. Note that elites are not subject to mutations. After the mutation, the process is restarted at the elitism stage until the maximum fitness function is reached. The search parameters in the GA are given in Table 6.

## 4. Case study

The helicopter tail rotor driveline presented by Zinberg and Symonds [1] is investigated with the GA. The original driveline, having a total length of 7.41 m, which is assumed to transmit a power of 447.4 kW, is composed of five subcritical aluminium alloy tubes and four intermediate supports. Zinberg and Symonds suggested replacing the conventional driveline by three subcritical composite shafts consisting of BE material. The properties of this composite shaft are compared with those of the aluminium one in Table 7. Note that the Zinberg shaft was obtained only on the basis of physical considerations.

In line with Lim and Darlow [3], who studied the same driveline case, the mass moment of inertia of the main gearing and tail rotor are assumed to be equal to  $0.94 \text{ kg m}^2$  and  $3.76 \text{ kg m}^2$ , respectively. To take the difference between the connections in the metallic and composite shafts into account, a weight penalty of 1.5 kg per composite shaft is added here.

### 4.1. Subcritical shaft optimisation

Subcritical shaft optimisation was first studied with the GA. The case of two single-carbon fibre/epoxy composites (BE and HM) and

Table 5: Reserve factors and penalisation factors

$K_{str}$	$K_{buck}$	$K_{tsupn}$	$K_{tinf n}$	$K_{fsup n}$	$K_{finf n}$	$K_{th}$	$\gamma_{1,2}$	$\gamma_3$	$\gamma_{j \notin \{1,2,3\}}$
0.44	0.44	0.83	1.15	0.8	1.2	0.8	2	6	4

Table 7: Optimised composite tail rotor driveline under subcritical conditions in comparison with the conventional aluminium driveline

Material			Conv.	Zinberg		Optimised		
			aluminium	BE[1]	BE	HM	HM <sup>b</sup>	HS/HM
Number of tubes	-		5			3		
String length	bit		-	-	24	24	30	30
Stacking sequence (from inner to outer radius)	°		-	[90,45, -45,0 <sub>6</sub> , 90]	[90 <sub>2</sub> ,0 <sub>4</sub> , -45,45, 90]	[90,0 <sub>3</sub> , 45,-45 <sub>2</sub> , 45]	[90,-22.5 <sub>2</sub> , 22.5,-22.5, 22.5 <sub>2</sub> ,-67.5]	[90 <sup>HM</sup> ,45 <sup>HR</sup> , 0 <sup>HM</sup> ,-45 <sup>HR</sup> , 90 <sup>HM</sup> ]
Operating speed	$\Omega_{nom}$	rev / min	5 540	4 320	3 800	4 800	4 600	4 400
1st critical speed	$\omega_1$	rev / min	8 887	5 697 <sup>a</sup>	4 606	5 800	5 695	5344
1st torsion mode	$\omega_1$	rev / min	2 058 <sup>a</sup>	1 292 <sup>a</sup>	1 065	1 534	1 254	635
2nd torsion mode	$\omega_2$	rev / min	65 370 <sup>a</sup>	35 318 <sup>a</sup>	36 428	64 965	59 599	34 510
Nominal torque	$T_{nom}$	N m	771	989	1 124	891	929	971
Strength torque	$T_{str}$	N m	4 925 <sup>a</sup>	4 880 <sup>a</sup>	3 149	2 268	2 267	3 349
Buckling torque	$T_{buck}$	N m	3 090 <sup>a</sup>	2 671 <sup>a</sup>	2 645	2 108	2 105	2 206
Tube length	$l$	m	1.482			2.470		
Mean tube radius	$r_m$	mm	56.3	62.84	56	54	50	46
Tube thickness	$t_s$	mm	1.65	1.321	1.19	1.00	1.00	1.00
Tubes weight	$N_s m_s$	kg (%)	13.38	8.16 (61)	6.09 (46)	4.26 (32)	3.96 (30)	3.57 (27)
Supports weight	$N_b m_b$	kg	15.42	7.71	9.68	8.24	8.48	8.75
Weight penalty		kg	-	4.5 <sup>a</sup>	4.5	4.5	4.5	4.5
Total weight	$m_{dv}$	kg	28.80	20.37 <sup>a</sup>	20.27	17	16.95	16.82
Weight saving		kg (%)	-	8.4 (29) <sup>a</sup>	8.5 (30)	11.8 (41)	11.9 (41)	12.0 (42)

<sup>a</sup> Value computed with presented methods. <sup>b</sup> with  $\text{bit}_\alpha = 3$

one hybrid case (HM/HS) was examined (see Table 1 for the properties of the materials). The optimisation procedure was computed six times with each composites to check that convergence of the GA was reached. The results of the optimisation are shown in Fig. 4 and the properties of the fittest individuals are summarise in Table 7 in each case. Figs. 4a-4d show the fitness function of the highest ranking individual during the evolution (number of generations) in six different populations. The legend gives the properties of the fittest individual in each population at the last generation. The results obtained show that the five conventional shafts can be replaced by three subcritical boron or carbon reinforced epoxy shafts. The algorithm did not find any subcritical solutions with only two shafts. We note that the operating speed was much higher than the first natural torsional frequency in all the solutions.

In the BE case (Fig. 4a), GA yielded three different solutions with the same fitness after 2000 generations. All the solutions gave the same radius, the same operating speed and the same plies (three 90° plies, four 0° plies, one -45° ply and one 45° ply) but various stacking sequence orders. They also gave the same critical speeds and the same strength. The independence of critical speed computations from the stacking sequence order is due to EMBT. As far as the strength is concerned, this independence results from in-plane shear loading and the assumption that uncoupled tension-bending is involved ( $\mathbf{B} = \mathbf{0}$ ). On the other hand, torsional buckling depends on the stacking sequence order, as shown in Table 4. In particular, the circumferential flexural stiffness of the laminate was found to be highly significant. This explains the position of the 90° plies, which are located in the inner and outer parts of the tube. The solution with the greatest buckling torque was selected as the best individual. The stacking sequence obtained ([90<sub>2</sub>, 0<sub>4</sub>, 45°, -45°, 90°]) was very

similar to that of Zinberg and Symonds's laminate ([90°, 45°, -45°, 0<sub>6</sub>, 90°]), only two 0° plies were replaced here by a 90° ply. The decrease in the shaft thickness and shaft radius explain the slight increase in weight saving from 29% to 30% obtained in comparison with the conventional aluminium shaft (see Table 7). The computing time required for one evolution was approximately equal to one hour using MATLAB [36] on a Xeon E5540.

The second material tested was HM carbon/epoxy (Fig. 4b). Convergence was reached after 200 generations, but five different solutions were obtained with the same fitness. Only the order between 0°, 45° and -45° plies and the operating speed were different. The optimum shaft stacking sequence maximising the strength and buckling margins was [90°, 0<sub>3</sub>, 45°, -45<sub>2</sub>, 45°]. This gives the minimum thickness authorized (1 mm). Due to the high level of stiffness in comparison with BE, only one 90° ply was necessary to prevent buckling and three 0° plies were required to avoid reaching the first critical speed. The number of  $\pm 45^\circ$  plies increased two-fold due to the low strength of HM carbon/epoxy. The weight saving increased considerably in comparison with the previous example, reaching 41% due to several combined effects: the decrease in the density, the mean tube radius, the thickness and the weight of the supports (due to the increase in the operating speed, see Eq. (16)).

The optimisation of the HM carbon/epoxy was then carried out with  $\text{bit}_\alpha = 3$  i.e.  $\alpha \in \{-67.5^\circ, -45^\circ, -22.5^\circ, 0^\circ, 22.5^\circ, 45^\circ, 67.5^\circ, 90^\circ\}$  (Fig. 4c). The chromosome length increased from 24 to 30. This considerably increased the search-space, and hence the number of generations required to obtain convergence and the computing time (approximately 3h/evolution). Convergence was obtained after approximately 6000 generations. Four different optimum individuals were obtained with the same fitness. All of them contained (+ and



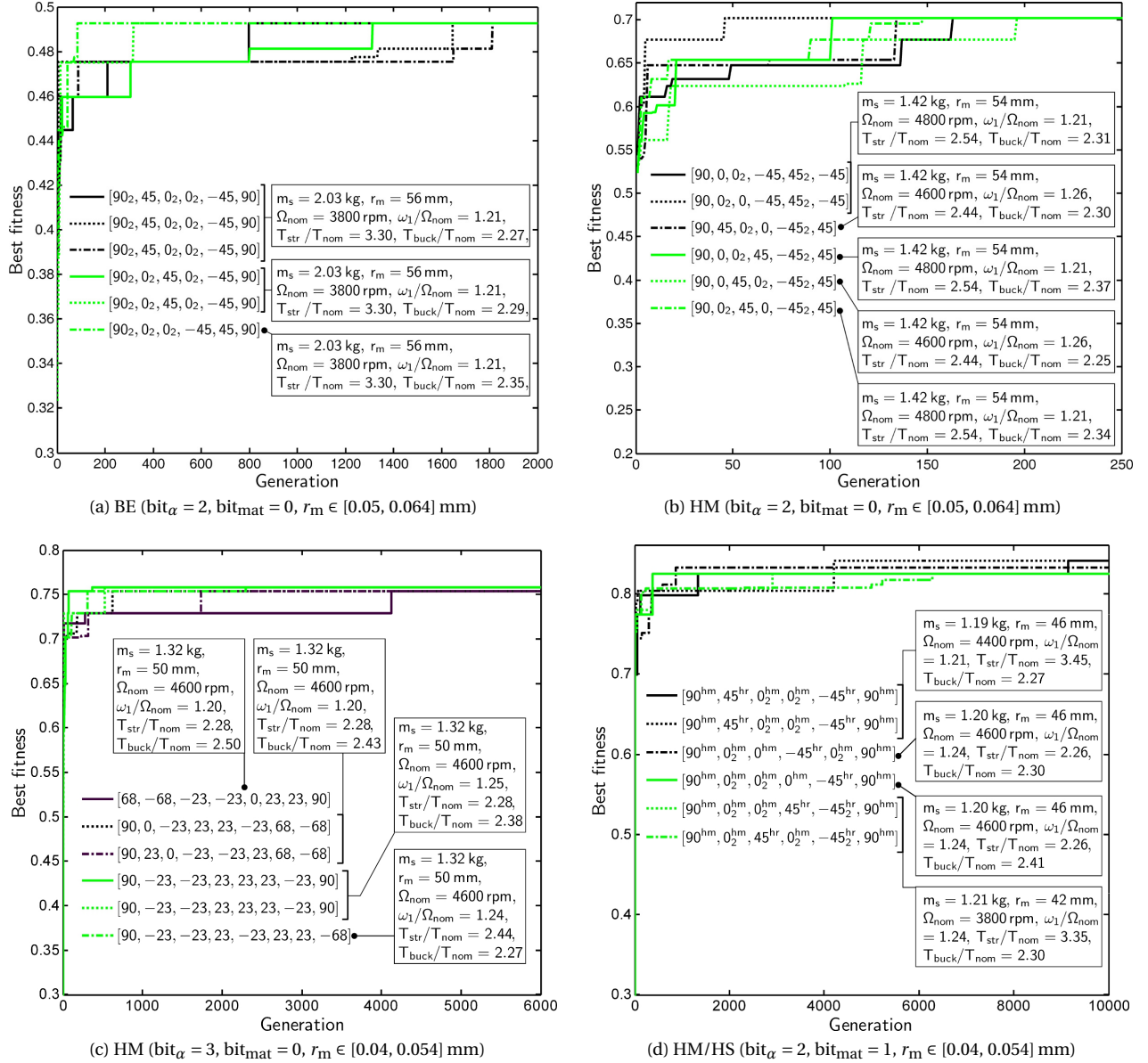


Figure 4: Evolution of the best individual fitness of several shaft populations in the case of various materials, subcritical conditions and three tubes forming the Zinberg and Symonds tail rotor driveline (there are 300 individuals in each evolution with  $\text{bit}_n = 1$ ,  $\text{bit}_{r_m} = 3$ ,  $\text{bit}_{\Omega_{\text{nom}}} = 3$ ,  $q = 6$ ,  $\Omega_{\text{nom}} \in [3800, 5200]$  rev / min,  $t_{s\text{min}} = 1$  mm and  $l = 2.470$  m)

-)22.5° plies, and most of them contained (+ and/or -)67.5° plies. The optimum shaft selected from four solutions was  $[90^\circ, -23^\circ_2, 23^\circ, -23^\circ, 23^\circ_2, -68^\circ]$ . This shaft did not contain  $0^\circ$  plies. The weight saving increased slightly in comparison with the previous case, mainly due to the decrease in the mean tube radius.

The last case tested was that of the hybrid HM/HS carbon/epoxy (Fig. 4d). Convergence was again obtained after approximately 6000 generations, despite the fact that only three evolutions yielded the optimum individual. The optimum stacking sequence obtained was  $[90^\circ_{\text{HM}}, 45^\circ_{\text{HR}}, 0^\circ_{\text{HM}}, -45^\circ_{\text{HR}}, 90^\circ_{\text{HM}}]$ . This result requires some simple comments. The  $90^\circ$  and  $0^\circ$  plies consisted of HM carbon/epoxy because these plies determine the stiffness problems (the dynamics and buckling). The  $\pm 45^\circ$  plies consisted of HS fibres because these plies determine the strength problem. The weight reduction obtained in comparison with the HM case was lower than expected. In fact, the decrease in the weight of the shaft was practically balanced by the increase in the weight of the supports.

The optimisation procedure was also carried out in the case of HS carbon/epoxy material (results not presented here). In the configuration studied here, the HS carbon/epoxy material gave a fitness score in between that obtained with BE and HM composite materials, due to its low density.

In addition, it is worth noting that the number of generations required to converge on the global optimum depended on the size of the search-space, as well as on the basin of attraction of the local and global optima. For example in the case of two materials with the same chromosome length, the number of generations required to reach convergence increased from 250 to 2000 (Figs. 4a-4b).

#### 4.2. Supercritical shaft optimisation

The subcritical condition was then removed. The optimisation was performed in the case of one single-carbon fibre/epoxy composite (HM) and one hybrid composite (HM/HS). The results obtained here show that the five conventional shafts can be replaced

Table 8: Optimised composite tail rotor driveline under supercritical conditions in comparison with the conventional aluminium driveline

Material			Conv.	Lim			
			aluminium	CE <sub>L</sub> [3]	HM	HM/HS	HM/HS
Number of tubes	-		5	1	2	2	1
String length	bit		-	-	27	33	34
Stacking sequence (from inner to outer radius)	°		-	[0 <sub>64%</sub> , -62 <sub>4%</sub> , 90 <sub>32%</sub> ] <sub>s</sub>	[90,45, 0 <sub>2</sub> ,-45 <sub>2</sub> , 0,45]	[90 <sup>HM</sup> ,0 <sub>3</sub> <sup>HM</sup> , -45 <sup>HR</sup> ,0 <sub>2</sub> <sup>HM</sup> , 90 <sup>HM</sup> ]	[90 <sup>HR</sup> ,0 <sub>9</sub> <sup>HM</sup> , -45 <sup>HR</sup> ]
Operating speed	$\Omega_{nom}$	rev / min	5 540	6000	5 400	4 800	7 000
1st critical speed	$\omega_1$	rev / min	8 887	490	2 696	2 647	1 018
2nd critical speed	$\omega_2$	rev / min	-	1 913 <sup>a</sup>	10 784	10 589	4 072
3rd critical speed	$\omega_3$	rev / min	-	4 303 <sup>a</sup>	24 264	23 824	9 161
4th critical speed	$\omega_4$	rev / min	-	7 650 <sup>a</sup>	43 136	42 355	16 287
1st torsion mode	$\omega_1$	rev / min	2 058 <sup>a</sup>	389 <sup>a</sup>	1 322	409	483
2nd torsion mode	$\omega_2$	rev / min	65 370 <sup>a</sup>	8 846 <sup>a</sup>	43 326	18 112	8 300
Threshold speed	$\omega_{th}$	rev / min	-	- <sup>b</sup>	23 658	20 356	13 638
Nominal torque	$T_{nom}$	N m	771	712	791	891	610
Strength torque	$T_{str}$	N m	4 925 <sup>a</sup>	1 492 <sup>a</sup>	2 439	2 096	4 352
Buckling torque	$T_{buck}$	N m	3 090 <sup>a</sup>	1 460 <sup>a</sup>	1 963	2 137	1 657
Tube length	$l$	m	1.482	7.41	3.705	3.705	7.41
Mean tube radius	$r_m$	mm	56.3	47.7	56.0	50.0	62.0
Tube thickness	$t_s$	mm	1.65	1.69	1.0	1.0	1.375
Support stiffness	$k_e$	kN m <sup>-1</sup>	-	- <sup>b</sup>	2 864	2 864	1 437
Tubes weight	$N_s m_s$	kg (%)	13.38	6.08 (45)	4.43 (33)	3.60 (27)	6.65 (50)
Supports weight	$N_b m_b$	kg	15.42	0	3.80	4.12	0
Weight penalty		kg	-	1.5	3.0	3.0	1.5
Total weight	$m_{dv}$	kg	28.80	7.58 <sup>a</sup>	11.23	10.72	8.15
Weight saving		kg (%)	-	21.22 (74)	17.6 (61)	18.1 (63)	20.7 (72)

<sup>a</sup> Value computed with presented methods. <sup>b</sup> Not under consideration in the reference.

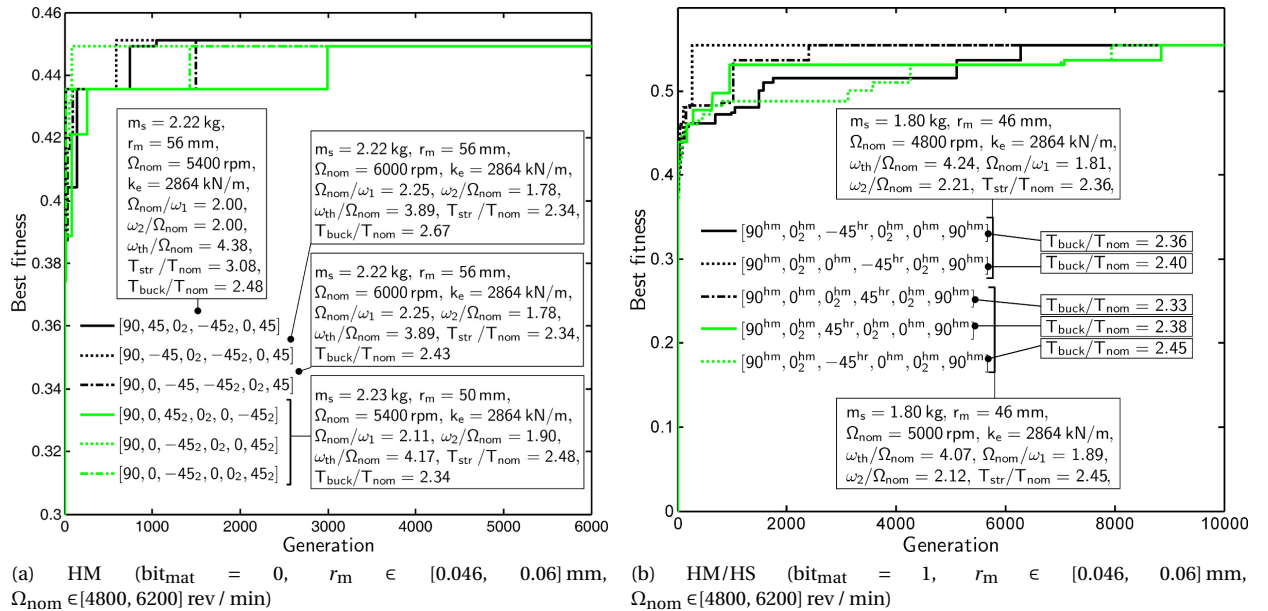


Figure 5: Evolution of the best individual fitness of several shaft populations in the case of various materials, supercritical conditions and two tubes forming the Zinberg and Symonds tail rotor driveline (there are 300 individuals in each evolution with  $bit_\alpha = 2$ ,  $bit_n = 1$ ,  $bit_{r_m} = 3$ ,  $bit_{k_e} = 3$ ,  $bit_{\Omega_{nom}} = 3$ ,  $q = 6$ ,  $k_e \in [10^4, 10^7]$  N m<sup>-1</sup>,  $t_{smin} = 1$  mm,  $\eta_e = 0.1$  and  $l = 3.705$  m)

by either one or two supercritical shafts (see Table 8 and Figs. 5-6). Contrary to the subcritical optimisation, it was necessary here to take the first four critical speeds and the threshold speed into ac-

count. The support stiffness was used as a supplementary optimisation variable to maximise the dynamic stability margin. Lim and Darlow [3] suggested optimising one shaft case with a carbon/epo-

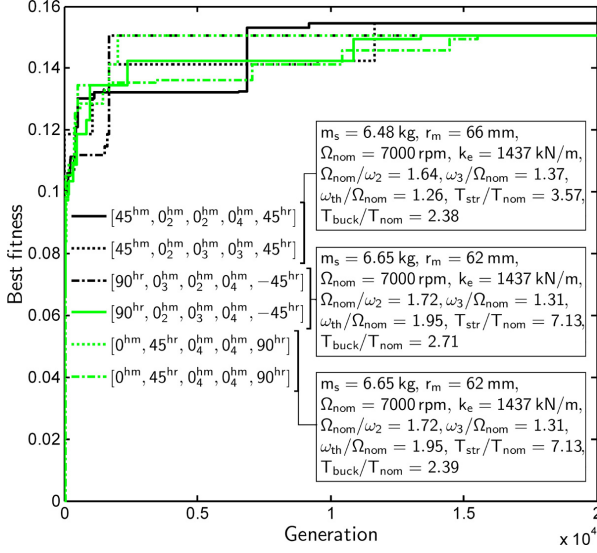


Figure 6: Evolution of the best individual fitness of several shaft populations in the case of HM/HS composite material, supercritical conditions and one tube forming the Zinberg and Symonds tail rotor driveline (there are 600 individuals in each evolution with  $bit_\alpha = 2$ ,  $bit_{mat} = 1$ ,  $bit_n = 2$ ,  $bit_{r_m} = 3$ ,  $bit_{k_e} = 3$ ,  $bit_{\Omega_{nom}} = 3$ ,  $q = 5$ ,  $r_m \in [0.052, 0.066]$  mm,  $\Omega_{nom} \in [5600, 7000]$  rev/min,  $k_e \in [10^4, 10^7]$  N m<sup>-1</sup>,  $t_{smin} = 1$  mm,  $\eta_e = 0.1$  and  $l = 7.410$  m)

xy composite denoted here CE<sub>L</sub> (Table 1). The latter authors used a generalised reduced gradient method involving continuous variables such as the fraction and the orientation of the laminate plies. Among the stacking sequences tested,  $[0^\circ_\alpha, \phi_{\beta p}, -\phi_{\beta n}, 90^\circ_\gamma]_s$ , the optimum one was  $[0^\circ_{64\%}, -62^\circ_{4\%}, 90^\circ_{32\%}]_s$  (Table 8). The operating speed was above the third critical speed and the dynamic stability was not taken into account.

In the two-tube case, the first material studied was HM carbon/epoxy (Fig. 5a). Convergence was reached with three populations after approximately 6 000 generations. The stacking sequence in the optimum shaft (involving larger margins) was  $[90^\circ, 45^\circ, 0^\circ_2, -45^\circ_2, 0^\circ, 45^\circ]$ . This sequence is the same as in the subcritical case, only the order is slightly different. The shaft radius increased from 54 to 56 mm. It can be seen from Fig. 5a that all the margins were particularly large ( $\geq 2$ ). In particular, the operating speed was in between the first and second critical speeds, and far above the threshold speed. Much greater weight saving was obtained here than with the conventional aluminium driveline (61%) or the optimum HM subcritical driveline, mainly due to the removal of one intermediate support.

The second case tested was that of the hybrid HM/HS carbon/epoxy (Fig. 5b). Five populations converged onto the optimum fitness after 10 000 generations. All the stacking sequences consisted of five  $0^\circ$  plies made of HM carbon/epoxy, two  $90^\circ$  plies made of HM carbon/epoxy, and one (+ or -) $45^\circ$  ply made of HS carbon/epoxy. The fittest individual was  $[90^\circ_{90}, 0^\circ_{90}, -45^\circ_{90}, 0^\circ_{90}, 90^\circ_{90}]$ . This outcome is similar to that obtained in the subcritical case, only one  $45^\circ_{HR}$  ply was replaced by one  $0^\circ_{HM}$  ply. The weight saving obtained was greater than in the HM fibre case, reaching 63%.

In the one-tube case, only hybrid HM/HS carbon/epoxy was studied (Fig. 6). Convergence was reached with five populations after approximately 20 000 generations. The stacking sequence corresponding to the optimum individual was  $[90^\circ_{HR}, 0^\circ_{90}, -45^\circ_{HR}]$ . It is worth noting that the number of  $0^\circ$  plies increased considerably in comparison with the two-tube case from 5 to 9, mainly due to the fact that the dynamic constraints had to be achieved. The operating speed here was in between the second and third critical speeds. The AG

selected HS fibres for the  $90^\circ$  ply here instead of HM fibres, which is unusual, possibly because the tube thickness was larger than in the previous cases tested, which reduced the buckling risk. The weight saving amounted here to 72%, which is almost equal to that obtained by Lim and Darlow [3]. However, this solution is more efficient because the operating speed was above the second critical speed and the dynamic stability is ensured.

The above optimisation procedure was carried out with  $bit_\alpha = 3$ . Even after 40 000 generations with 8 populations of 600 individuals, AG did not come up with a better solution. In this case, the computing time was much longer, amounting to approximately 18 hours per population.

## 5. Conclusion

In this study, some assumptions and simplifications were adopted in order to describe the supercritical motion, the failure strength and the torsional buckling of a CFRP drive shaft sufficiently accurately. The GA presented for optimising supercritical drive shafts was tested on an example previously described in the literature. Analytical models are useful means of obtaining quite reasonable computing times. This example shows the value of CFRP shafts and in particular, that of hybrid CFRP shafts. These solutions make it possible to greatly decrease the number of shafts and the driveline weight under subcritical conditions and even more under supercritical conditions. In most of the cases studied, the following general rules emerged for defining the stacking sequence of hybrid solutions without requiring any optimisation algorithms:

1.  $\pm 45^\circ$  HS carbon/epoxy plies should be used in order to maximise the torque resistance, in variable proportions ranging between  $+45^\circ$  and  $-45^\circ$ , depending on the maximum torque direction;
2.  $0^\circ$  HM carbon/epoxy plies should be used in order to maximise the axial stiffness and minimise the axial damping involved in bending oscillations;
3.  $90^\circ$  HM carbon/epoxy plies should be used far from the shaft middle surface in order to maximise the torsional buckling torque;
4. the laminate does not generally have to be symmetrical.

## Appendix A. Torsional buckling equations

Equilibrium equations used to solve the torsional buckling problem in the case of a circular cylinder with orthotropic properties:

$$\begin{aligned}
& \left( A_{11} + \frac{B_{11}}{r} \right) u'' + \left( 2A_{13} - \frac{T}{\pi r^2} \right) u' \\
& + \left( A_{33} - \frac{B_{33}}{r} + \frac{D_{33}}{r^2} \right) \ddot{u} + \left( A_{13} + \frac{2B_{13}}{r} + \frac{D_{13}}{r^2} \right) v'' \\
& + \left( A_{12} + \frac{B_{12}}{r} + A_{33} + \frac{B_{33}}{r} \right) \dot{v}' + A_{23} \ddot{v} - \left( \frac{B_{11}}{r} + \frac{D_{11}}{r^2} \right) w'''' \\
& + A_{12} w' + \left( -\frac{B_{23}}{r} + \frac{D_{23}}{r^2} \right) \ddot{w} + \left( A_{23} - \frac{B_{23}}{r} + \frac{D_{23}}{r^2} \right) \dot{w} \\
& + \left( -\frac{B_{12}}{r} - \frac{2B_{33}}{r} + \frac{D_{33}}{r^2} \right) \dot{w}' - \left( \frac{3B_{13}}{r} + \frac{D_{13}}{r^2} \right) w'' = 0
\end{aligned} \tag{A.1}$$

$$\begin{aligned}
& \left( A_{13} + \frac{2B_{13}}{r} + \frac{D_{13}}{r^2} \right) u'' + \left( A_{12} + \frac{B_{12}}{r} + A_{33} + \frac{B_{33}}{r} - \frac{D_{33}}{2r^2} \right) \dot{u}' \\
& + \left( A_{23} + \frac{3D_{23}}{2r^2} \right) \ddot{u} + \left( A_{33} + \frac{3B_{33}}{r} + \frac{5D_{33}}{2r^2} \right) v'' \\
& + \left( 2A_{23} + \frac{4B_{23}}{r} + \frac{2D_{23}}{r^2} - \frac{T}{\pi r^2} \right) \dot{v}' + \left( A_{22} + \frac{B_{22}}{r} \right) \ddot{v} + A_{22} \dot{w} \\
& - \left( \frac{B_{13}}{r} + \frac{2D_{13}}{r^2} \right) w'' + \left( A_{23} + \frac{B_{23}}{r} - \frac{T}{\pi r^2} \right) w' - \frac{B_{22}}{r} \ddot{w} \\
& + \left( -\frac{B_{12}}{r} - \frac{D_{12}}{r^2} - \frac{2B_{33}}{r} - \frac{3D_{33}}{r^2} \right) \dot{w}' + \left( -\frac{3B_{23}}{r} + \frac{D_{23}}{r^2} \right) \dot{w} = 0 \quad (A.2)
\end{aligned}$$

$$\begin{aligned}
& \left( \frac{B_{11}}{r} + \frac{D_{11}}{r^2} \right) u'' + \left( 3\frac{B_{13}}{r} + \frac{D_{13}}{r^2} \right) \dot{u}'' \\
& + \left( 2\frac{B_{33}}{r} - \frac{D_{33}}{r^2} + \frac{B_{12}}{r} \right) \ddot{u}' + \left( \frac{B_{23}}{r} - \frac{D_{23}}{r^2} \right) \ddot{u} - A_{12} u' \\
& + \left( -A_{23} + \frac{B_{23}}{r} - \frac{D_{23}}{r^2} \right) \dot{u} + \left( \frac{B_{13}}{r} + \frac{2D_{13}}{r^2} \right) v'' \\
& + \left( 2\frac{B_{33}}{r} + \frac{3D_{33}}{r^2} + \frac{B_{12}}{r} + \frac{D_{12}}{r^2} \right) \dot{v}' + \left( 3\frac{B_{23}}{r} + \frac{2D_{23}}{r^2} \right) \dot{v} \\
& + \frac{B_{22}}{r} \ddot{v} + \left( -A_{23} - \frac{B_{23}}{r} + \frac{T}{\pi r^2} \right) v' - A_{22} \dot{v} - \frac{D_{11}}{r^2} w'' \\
& - \frac{4D_{13}}{r^2} \dot{w}'' - \left( \frac{4D_{33}}{r^2} + 2\frac{D_{12}}{r^2} \right) \dot{w}' - \frac{4D_{23}}{r^2} \dot{w} \\
& - \frac{D_{22}}{r^2} \ddot{w} + \frac{3B_{12}}{r} w'' + \left( \frac{4B_{23}}{r} - \frac{2D_{23}}{r^2} - \frac{T}{\pi r^2} \right) \dot{w}' \\
& + \left( \frac{2B_{22}}{r} - \frac{2D_{22}}{r^2} \right) \dot{w} + \left( -A_{22} + \frac{B_{22}}{r} - \frac{D_{22}}{r^2} \right) w = 0 \quad (A.3)
\end{aligned}$$

where  $' = r \partial / \partial x$  and  $\dot{\phantom{x}} = \partial / \partial \varphi$ .

Elements of the stiffness matrix in the torsional buckling problem in the case of a very long circular cylinder with orthotropic properties:

$$\begin{aligned}
K(1,1) &= - \left( A_{11} + \frac{B_{11}}{r} \right) \lambda^2 - \left( 2A_{13} - \frac{T}{\pi r^2} \right) h \lambda \\
& - \left( A_{33} - \frac{B_{33}}{r} + \frac{D_{33}}{r^2} \right) h^2 \quad (A.4)
\end{aligned}$$

$$\begin{aligned}
K(1,2) &= - \left( A_{13} + \frac{2B_{13}}{r} + \frac{D_{13}}{r^2} \right) \lambda^2 \\
& - \left( A_{12} + \frac{B_{12}}{r} + A_{33} + \frac{B_{33}}{r} \right) h \lambda - A_{23} h^2 \quad (A.5)
\end{aligned}$$

$$\begin{aligned}
K(1,3) &= - \left( \frac{B_{11}}{r} + \frac{D_{11}}{r^2} \right) \lambda^3 + A_{12} \lambda \\
& + \left( -\frac{B_{23}}{r} + \frac{D_{23}}{r^2} \right) h^3 + \left( A_{23} - \frac{B_{23}}{r} + \frac{D_{23}}{r^2} \right) h \\
& + \left( -\frac{B_{12}}{r} - \frac{2B_{33}}{r} + \frac{D_{33}}{r^2} \right) h^2 \lambda - \left( \frac{3B_{13}}{r} + \frac{D_{13}}{r^2} \right) h \lambda^2 \quad (A.6)
\end{aligned}$$

$$\begin{aligned}
K(2,1) &= - \left( A_{13} + \frac{2B_{13}}{r} + \frac{D_{13}}{r^2} \right) \lambda^2 \\
& - \left( A_{12} + \frac{B_{12}}{r} + A_{33} + \frac{B_{33}}{r} - \frac{D_{33}}{2r^2} \right) h \lambda - \left( A_{23} + \frac{3D_{23}}{2r^2} \right) h^2 \quad (A.7)
\end{aligned}$$

$$\begin{aligned}
K(2,2) &= - \left( A_{33} + \frac{3B_{33}}{r} + \frac{5D_{33}}{2r^2} \right) \lambda^2 \\
& - \left( 2A_{23} + \frac{4B_{23}}{r} + \frac{2D_{23}}{r^2} - \frac{T}{\pi r^2} \right) h \lambda - \left( A_{22} + \frac{B_{22}}{r} \right) h^2 \quad (A.8)
\end{aligned}$$

$$\begin{aligned}
K(2,3) &= - \left( \frac{B_{13}}{r} - \frac{2D_{13}}{r^2} \right) \lambda^3 + \left( A_{23} + \frac{B_{23}}{r} - \frac{T}{\pi r^2} \right) \lambda \\
& - \frac{B_{22}}{r} h^3 + A_{22} h + \left( -\frac{3B_{23}}{r} + \frac{D_{23}}{r^2} \right) h^2 \lambda \\
& - \left( \frac{B_{12}}{r} + \frac{D_{12}}{r^2} + \frac{2B_{33}}{r} + \frac{3D_{33}}{r^2} \right) h \lambda^2 \quad (A.9)
\end{aligned}$$

$$\begin{aligned}
K(3,1) &= - \left( \frac{B_{11}}{r} + \frac{D_{11}}{r^2} \right) \lambda^3 - \left( 3\frac{B_{13}}{r} + \frac{D_{13}}{r^2} \right) h \lambda^2 \\
& - \left( 2\frac{B_{33}}{r} - \frac{D_{33}}{r^2} + \frac{B_{12}}{r} \right) h^2 \lambda \\
& - \left( \frac{B_{23}}{r} - \frac{D_{23}}{r^2} \right) h^3 - A_{12} \lambda + \left( -A_{23} + \frac{B_{23}}{r} - \frac{D_{23}}{r^2} \right) h \quad (A.10)
\end{aligned}$$

$$\begin{aligned}
K(3,2) &= - \left( \frac{B_{13}}{r} + \frac{2D_{13}}{r^2} \right) \lambda^3 \\
& - \left( 2\frac{B_{33}}{r} + \frac{3D_{33}}{r^2} + \frac{B_{12}}{r} + \frac{D_{12}}{r^2} \right) h \lambda^2 - \left( 3\frac{B_{23}}{r} + \frac{2D_{23}}{r^2} \right) h^2 \lambda \\
& - \frac{B_{22}}{r} h^3 + \left( -A_{23} - \frac{B_{23}}{r} + \frac{T}{\pi r^2} \right) \lambda - A_{22} h \quad (A.11)
\end{aligned}$$

$$\begin{aligned}
K(3,3) &= - \frac{D_{11}}{r^2} \lambda^4 - \frac{4D_{13}}{r^2} h \lambda^3 - \left( \frac{4D_{33}}{r^2} + 2\frac{D_{12}}{r^2} \right) h^2 \lambda^2 \\
& - \frac{4D_{23}}{r^2} h^3 \lambda - \frac{D_{22}}{r^2} h^4 - \frac{3B_{12}}{r} \lambda^2 - \left( \frac{4B_{23}}{r} - \frac{2D_{23}}{r^2} - \frac{T}{\pi r^2} \right) h \lambda \\
& - \left( \frac{2B_{22}}{r} - \frac{2D_{22}}{r^2} \right) h^2 + \left( -A_{22} + \frac{B_{22}}{r} - \frac{D_{22}}{r^2} \right) \quad (A.12)
\end{aligned}$$

where  $\lambda = p\pi r/l$ .

## References

- [1] H. Zinberg, M. E. Symonds, The Development of an Advanced Composite Tail Rotor Driveshaft, in: Proceedings of the 26th Annual Forum of the American Helicopter Society, Washington, United States, 1970.
- [2] O. A. Bauchau, Optimal design of high speed rotating graphite/epoxy shafts, *Journal of Composite Materials* 17 (3) (1983) 170–181.
- [3] J. W. Lim, M. S. Darlow, Optimal sizing of composite power transmission shafting, *Journal of the American Helicopters society* 31 (1986) 75–83.
- [4] M. S. Darlow, J. Creonte, Optimal design of composite helicopter power transmission shafts with axially varying fiber lay-up, *Journal of the American Helicopters society* 40 (2) (1995) 50–56.
- [5] H. B. H. Gubran, K. Gupta, Composite Shaft Optimization Using Simulated Annealing, Part I: Natural Frequency, *International Journal of Rotating Machinery* 8 (4) (2002) 275–283.
- [6] D. Goldberg, *Genetic Algorithms*, Addison Wesley, 1989.
- [7] Z. Awad, T. Aravinthan, Y. Zhuge, F. Gonzalez, A review of optimization techniques used in the design of fibre composite structures for civil engineering applications, *Materials & Design* 33 (2012) 534–544.
- [8] C. Roos, C. E. Bakis, Multi-Physics Design and Optimization of Flexible Matrix Composite Driveshafts, *Composite Structures* 93 (9) (2011) 2231–2240.
- [9] E.-J. Xu, J.-R. Ye, Y.-D. Xue, Design and Mechanical Analysis of a Hybrid Composite Driveshaft, *Composite Structures* 9 (1991) 207–216.
- [10] H. B. H. Gubran, Dynamics of hybrid shafts, *Mechanics Research Communications* 32 (4) (2005) 368–374.
- [11] M. A. Badie, E. Mahdi, A. M. S. Hamouda, An investigation into hybrid carbon/glass fiber reinforced epoxy composite automotive drive shaft, *Materials & Design* 32 (3) (2011) 1485–1500.
- [12] D. G. Lee, H. S. Kim, J. W. Kim, J. K. Kim, Design and manufacture of an automotive hybrid aluminum/composite drive shaft, *Composite Structures* 63 (2004) 87–99.
- [13] S. A. Mutasher, Prediction of the torsional strength of the hybrid aluminum/composite drive shaft, *Materials & Design* 30 (2) (2009) 215–220.
- [14] A. Abu Talib, A. Ali, M. Badie, N. Azida Che Lah, A. Golestaneh, Developing a hybrid, carbon/glass fiber-reinforced, epoxy composite automotive drive shaft, *Materials & Design* 31 (1) (2010) 514–521.
- [15] C. Hochard, J. Payan, O. Montagnier, Design and computation of laminated composite structures, *Composites Science and Technology* 65 (2005) 467–474.

- [16] O. Montagnier, C. Hochard, Compression characterization of high modulus carbon fibers, *Journal of Composite Materials* 39 (2005) 35–49.
- [17] J. K. Dutt, B. C. Nakra, Stability characteristics of rotating systems with journal bearings on viscoelastic support, *Mechanism and Machine Theory* 31 (6) (1996) 771–779.
- [18] O. Montagnier, C. Hochard, Dynamic instability of supercritical driveshafts mounted on dissipative supports – effect of viscous and hysteretic internal damping, *Journal of Sound and Vibration* 305 (2007) 378–400.
- [19] C. W. Bert, C. K. Kim, Whirling of composite material driveshafts including bending-twisting coupling and transverse shear deformation, *Journal of Vibration and Acoustics* 117 (1) (1995) 7–21.
- [20] H. B. H. Gubran, K. Gupta, The effect of stacking sequence and coupling mechanisms on the natural frequencies of composite shaft, *Journal of Sound and Vibration* 282 (1-2) (2005) 231–248.
- [21] R. Sino, T. N. Baranger, E. Chatelet, G. Jacquet, Dynamic analysis of a rotating composite shaft, *Composites Science and Technology* 68 (2) (2008) 337–345.
- [22] S. Timoshenko, *Vibration problems in engineering*, D. Van Nostrand company, inc., 1937.
- [23] S. Tsai, H. Hahn, *Introduction to composite materials*, CRC, 1980.
- [24] R. D. Adams, *Engineering Material Handbook*, vol. 1, chap. Damping properties analysis of composites, ASME, 206–217, 1987.
- [25] O. Montagnier, *Tubes composites à grande vitesse de rotation : analyses expérimentales et modélisation*, Ph.D. thesis, University of Marseille, France, 2005.
- [26] R. D. Adams, D. G. C. Bacon, Effect of fiber orientation and laminate geometry on the dynamic properties of the C.F.R.P., *Journal of Composite Materials* 7 (1973) 422–428.
- [27] R. G. Ni, R. D. Adams, A rational method for obtaining the dynamic mechanical properties of laminae for prediction of the damping of laminated plates and beams, *Composites* 15 (3) (1984) 193–199.
- [28] O. Montagnier, C. Hochard, Experimental investigation of dynamic instability of supercritical driveshafts due to internal damping, in: *Proceedings of the 7th IFToMM – Conference on Rotor Dynamics*, Vienna, Austria, 2006.
- [29] S. W. Tsai, E. M. Wu, A general theory of strength of anisotropic materials, *Journal of Composite Materials* 5 (1971) 58–69.
- [30] C. Hochard, S. Miot, N. Lahellec, F. Mazerolle, M. Herman, J. Charles, Behaviour up to rupture of woven ply laminate structures under static loading conditions, *Composites Part A* 40 (8) (2009) 1017–1023.
- [31] T. Hayashi, Optimization of the Torsional-Rigidity and Strength for Fiber Reinforced Composite Cylinders, in: *Proceedings of the Conference on Composite Materials*, vol. 1, 703–724, 1975.
- [32] W. Flügge, *Stresses in shells*, Springer-Verlag, Berlin, 2nd edn., 1973.
- [33] C. Bert, C.-D. Kim, Analysis of buckling of hollow laminated composite drive shaft, *Composites Science and Technology* 53 (1995) 343–351.
- [34] K. Hibbitt, I. Sorensen, *ABAQUS/Standard: User's Manual*, Hibbitt, Karlsson & Sorensen, 2001.
- [35] O. A. Bauchau, T. M. Krafchack, J. F. Hayes, Torsional Buckling Analysis and Damage Tolerance of Graphite/Epoxy Shafts, *Journal of Composite Materials* 22 (1988) 258–270.
- [36] The MathWorks, MATLAB, The MathWorks Inc., <http://www.mathworks.com>, 1990.